Formation of miscible fluid microstructures by hydrodynamic focusing in plane geometries

Thomas Cubaud[1,*] and Thomas G. Mason[2]

[1]*Department of Mechanical Engineering, Stony Brook University, Stony Brook, New York 11794, USA*
[2]*Department of Chemistry and Biochemistry, Department of Physics and Astronomy, and California NanoSystems Institute,*
University of California Los Angeles, Los Angeles, California 90095, USA

We experimentally investigate the flow structures formed when two miscible fluids that have large viscosity contrasts are injected and hydrodynamically focused in plane microchannels. Parallel viscous flows composed of a central stream surrounded by symmetric sheath streams are examined as a function of the flow rates, fluid viscosities, and rates of molecular diffusion. We study miscible interfacial morphologies and show a route for manipulating viscous flow-segregation processes in plane microsystems. The diffusion layer at the boundary of an ensheathed fluid grows as function of the distance downstream and depends on the Péclet number. In particular, we observe diffusion-enhanced viscous ensheathing processes. In the presence of a constriction, we investigate the formation of a lubricated viscous thread in the converging flow and also the buckling morphologies of the thread in the diverging flow. This study, relevant to multifluid flow between a "thick" material and a "thin" solvent, demonstrates the possibility to further control steady and oscillatory miscible fluid microstructures.

PACS number(s): 47.61.−k, 47.55.Hd, 47.55.Iv, 47.55.pd

I. INTRODUCTION

Miscible multifluid flow provides a powerful basis for performing chemical reactions at the microscale [1–3]. Convection-diffusion mechanisms associated with streams of diluted suspensions having small viscosity contrasts have been extensively studied for the formation of longitudinal or transverse diffusion gradients [4–6] as well as for improving micromixing [7–9]. However, large molecules and concentrated particulates can substantially increase the viscosity of a stream and therefore modify multifluid dynamics. The transport and synthesis of "thick" (i.e., highly viscous) materials in microsystems represent major challenges due to high flow resistance and also to the difficulty in manipulating interfaces with "thin" (i.e., less viscous) liquids, such as solvents. Although the stability of viscosity-stratified flows [10–13] and miscible displacements [14–17], resulting in the formation of viscous fingers and spikes, have been extensively studied, the behavior of miscible multifluid flows having large viscosity contrasts have only been minimally covered in microgeometries [18,19]. Indeed, such flows involve complex dynamics of interfacial free boundaries as well as diffusive transport and intermixing at those boundaries, thereby precluding a simple theoretical description. However, an important characteristic of these flows is the tendency for low-viscosity constituents to place themselves in the region of high shear and thereby consequently envelop high-viscosity constituents [20–22]. This material encapsulation, ensheathing, or self-lubrication property offers a promising means for manipulating fluid interfaces and reducing the hydraulic resistance in micro- and nanofluidic devices.

Hydrodynamic focusing is a technique commonly used for controlling a sample stream using sheath flows [23]. The sample liquid is introduced from a central channel, and flows that ensheath the sample liquid are introduced from side channels. Downstream from the junction, the fluids flow side by side, and the width and location of the sample stream can be controlled through the injection flow rates. Various flow-geometry relationships have been studied to create specific effects, including the influence of the channel aspect ratio [24], the injection geometry for detaching the central stream from the walls [25,26], the fluid driving mechanisms [27], and the effect of small [28] and moderate [29] viscosity contrasts between the fluids. Hydrodynamic focusing techniques also reveal the influence of diffusion on microflows. For miscible liquids having small viscosity contrast and flowing concurrently in plane microchannels with a gap h, the diffusion width or fluid mixing layer δ spreads differently near the top and bottom walls, and near the channel middle plane due the parabolic Stokes flow. The Péclet number $\mathrm{Pe}=Uh/D$, where U is the interface velocity and D is the molecular diffusion coefficient, compares the relative influence of convection and diffusion. When $X/\mathrm{Pe}\ll1$, where $X=x/h$ is the dimensionless downstream distance and x is the axial length from the fluid junction, experimental and theoretical investigations [30–32] have shown that the diffusion layer spreads as $\delta/h \propto (X/\mathrm{Pe})^{1/3}$. This weakly diffusive regime is characteristic of the "upstream region" where diffusion occurs predominantly near the walls. When $X/\mathrm{Pe}\gg1$, the diffusion layer spreads as $\delta/h \propto (X/\mathrm{Pe})^{1/2}$. This regime is strongly diffusive and typical of the "downstream" region or Taylor dispersion. The crossover occurs when the transverse extension of the diffusion layer $\delta \sim h$. In the presence of large viscosity contrasts, however, encapsulation effects and fluid mixing induce complex viscosity gradients, which affect the velocity field and the flow microstructure.

Here, we experimentally investigate two-fluid miscible flow behaviors in the presence of large viscosity contrasts in plane microchannels using hydrodynamic focusing. Gray-scale profile analysis of the transmitted light that is microscopically imaged using a fast camera enables us to deter-

*Author to whom correspondence should be addressed. thomas.cubaud@stonybrook.edu

mine miscible interface morphologies and the evolution of the diffusion layers in the upstream and downstream regions. First, when diffusion effects are negligible, we study the influence of flow rates and fluid viscosities on the central stream width. Then, we focus on the case of a more viscous central stream and show that strong molecular diffusion favors viscous encapsulation. Finally, we investigate the effect of a constriction on self-lubrication processes and show the onset of viscous buckling instabilities in the diverging flow region downstream from the constriction after a viscous thread is formed. In this case, we show that the primary deformation can undergo a secondary coiling or folding depending on the Péclet number. Overall, this study reveals and quantifies mechanisms associated with transporting and mixing high-viscosity and low-viscosity fluids in plane micro-geometries.

II. EXPERIMENTAL APPARATUS

We use conventional polydimethylsiloxane (PDMS) oils (i.e., silicone oils) having a wide range of viscosities, $0.82 \leq \eta \leq 500$ cP. Over the range of flow rates investigated (corresponding to shear rates $<10^4$ s^{-1}), these oils behave like Newtonian fluids. Since the silicone oils differ only in their molecular weights M (i.e., in their degrees of polymerization), the molecular diffusion coefficient D for a given fluid pair can be determined using a reference oil pair, having approximately $D \approx 2.6 \times 10^{-10}$ m^2 s^{-1} for the viscosities $\eta_S = 0.82$ cP for the thin oil and $\eta_L = 1030$ cP for the thick oil [33]. For large molecular size ratio between the liquids (i.e., for large viscosity contrast $\eta_L/\eta_S \gg 1$), the product $D\eta_S\theta$, where θ is the molecule hydrodynamic radius of the thick oil, remains constant at fixed temperature according to the Stokes-Einstein relation [34]. For PDMS oils, the mean radius of gyration of the entangled polymer chain, $\langle S \rangle$, is proportional to the molecule hydrodynamic radius θ [35] and its mean square radius scales as $\langle S^2 \rangle = aM^b$, with $a = 0.0666$ and $b = 1.0141$ [36]. For the range of viscosity used in the experiments, we calculate from the manufacturer's data sheet (Gelest) that $\eta_L \propto M^{1.47}$. Therefore, the molecule hydrodynamic radius of the thick oil is assumed to scale as $\theta \propto \eta_L^k$ with $k = 0.34$, and the product $D\eta_S\eta_L^k$ should remain essentially constant. This method allows for estimating D for a given oil pair using the reference oil pair. For instance, we estimate $D \approx 5.74 \times 10^{-9}$ m^2 s^{-1} for a fluid pair having the viscosities $\eta = 0.82$ and 100 cP. For the fluid pairs investigated, the diffusion coefficients D range between 1.49×10^{-9} and 4.5×10^{-11} m^2 s^{-1}. The silicone oils used in this study have similar refractive indexes, n, which range between 1.38 and 1.40.

Glass/silicon/glass "sandwich" microchannels are constructed in a clean room environment following standard procedures of microlithography, deep reactive ion etching, and anodic bonding [18]. In order to fabricate transparent devices, we etch through a thin, double-side-polished silicon wafer of thickness $h = 100$ μm and anodically bond borosilicate glass plates on each side of the silicon slab. As a result, the glass plates form the top and bottom walls of the microchannel, and the silicon forms the sidewalls (Fig. 1). Each channel is fed independently with fluids that are injected into
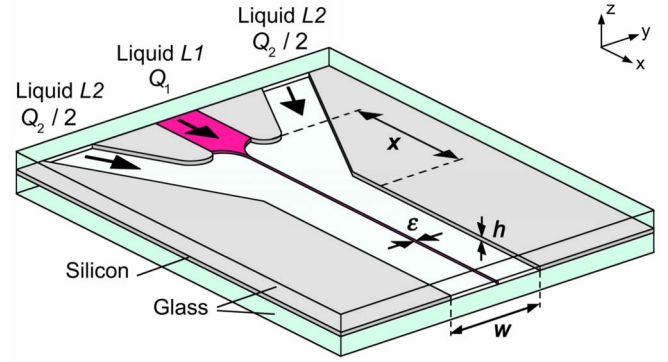

FIG. 1. (Color online) Schematic of viscous hydrodynamic focusing in a plane straight geometry with a plate gap $h = 100$ μm, and a terminal downstream width $w = 2$ mm.

the device with mechanical syringe pumps. These transparent devices advantageously provide facile visualization of miscible interfaces using high-intensity light in transmission without addition of dye or particulates. A fiber-optic bundle connected to a 150 W halogen bulb is placed at 10 cm from the microchannel to provide a collimated light source that is homogeneous and bright enough for high-speed digital imaging. On the opposite side of the microchannel, a high-speed camera equipped with a microlens and an extension tube captures digital images and movies, which are analyzed to determine the flow characteristics associated with a given channel geometry, fluid pair, and injection rates.

III. CENTRAL STREAM WITH LARGE VISCOSITY CONTRAST IN A PLANE STRAIGHT GEOMETRY

A. Velocity contrast

The microchannel design consists of a plane hydrodynamic focusing geometry of height $h = 100$ μm in the z axis with three inlet channels of width $w_i = 1$ mm that intersect with an angle of 22° and are connected with circular walls. The liquid 1 ($L1$), having a viscosity η_1, is injected from the central channel with a flow rate Q_1 and the liquid 2 ($L2$), having a viscosity η_2, is symmetrically injected from the side channels with a total flow rate Q_2. The outlet channel reaches a constant width $w = 2$ mm along the y axis, from the fluid contact region in the x axis after a distance $L_i = 2.2$ mm such that $L_i \sim w$ (Fig. 1). The large channel aspect ratio, $w/h = 20$, allows for comparing flow behaviors with a Hele-Shaw cell approximation [37]. Away from the sidewalls and $L1/L2$ interface, the Stokes equations for the bulk of each region are reduced to $\eta(\partial^2 U)/(\partial z^2) = (\partial P)/(\partial x)$, where U is the velocity and P the pressure. Therefore, the velocity profile is parabolic on the z axis and the average or bulk velocity U^* follows $12\eta U^*/h^2 = -(\partial P)/(\partial x)$. Assuming a constant pressure in the z-y plane, the bulk velocities U_1^* in $L1$ and U_2^* in $L2$ are related to the viscosities by

$$\eta_1 U_1^* = \eta_2 U_2^*. \tag{1}$$

Examples of experimental flows with large viscosity contrasts are given in Fig. 2 along with a sketch of the mean
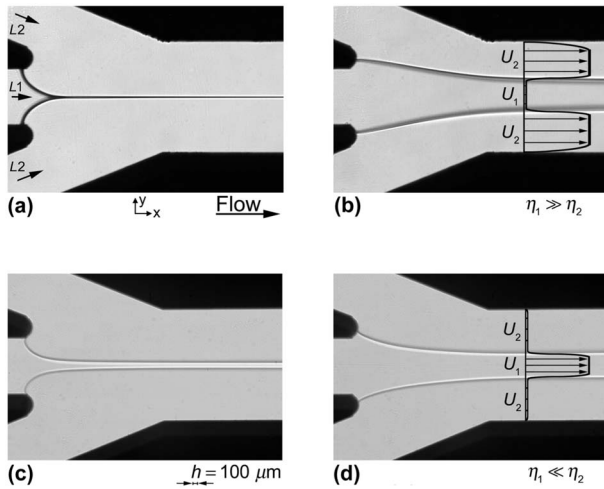
FIG. 2. Experimental micrographs of viscous hydrodynamic focusing in plane geometry with bulk velocity profiles. Viscosities in cP and flow rates in $\mu l \, min^{-1}$. (a) $Q_1=0.5$, $Q_2=1200$, $\eta_1=100$, $\eta_2=0.82$. (b) $Q_1=2$, $Q_2=600$, $\eta_1=100$, $\eta_2=0.82$. (c) $Q_1=20$, $Q_2=10$, $\eta_1=6$, $\eta_2=500$. (d) $Q_1=70$, $Q_2=8$, $\eta_1=6$, $\eta_2=500$.

velocity profile over the reasonable matching length h from the boundary conditions. Flows are stationary, yielding a well-defined interface between the miscible fluids. For a given viscosity ratio $\chi=\eta_1/\eta_2$, the width of the central stream ε can be adjusted through the flow rate ratio $\varphi=Q_1/Q_2$. For large viscosity contrasts, the bulk velocity of the more viscous liquid becomes negligible compared to the bulk velocity of the less viscous liquid. Therefore, although the boundary with the more viscous liquid is slowly moving, it acts almost as a solid wall (Fig. 2). This type system is promising for confining fluids into reconfigurable microchannels bounded by "viscous walls" that are adjusted with the rates of injection.

B. Miscible interface morphology

The previous analysis assumes a flat $L1/L2$ interface. However, due to the combination of the large bulk velocity contrasts [Eq. (1)] and the velocity continuity $U_1=U_2$ at the free surface, the system adjusts the fluid interface. In particular, as the less viscous liquid tends to drag the more viscous liquid, the more viscous liquid is also displaced in the y direction near the walls, i.e., in the direction transverse to the flow. As a result, the interface between two parallel miscible streams, having widely different viscosities, is curved. Figure 3 displays experimental grayscale profiles across a central stream for $\chi \ll 1$ and for $\chi \gg 1$. Analysis of the transmitted light intensity across the flow region gives useful information about the flow morphologies. Where the transmitted light is refracted by the curved interfaces, these regions appear darker compared to bulk fluid regions and are characterized by a valley in the grayscale. By contrast, nearby regions appear lighter due to the additional collected light deflected from the curved interface and are characterized by a peak in the grayscale. These regions are interpreted as areas where molecular diffusion is important. Although our bright-field experimental setup does not allow in principle
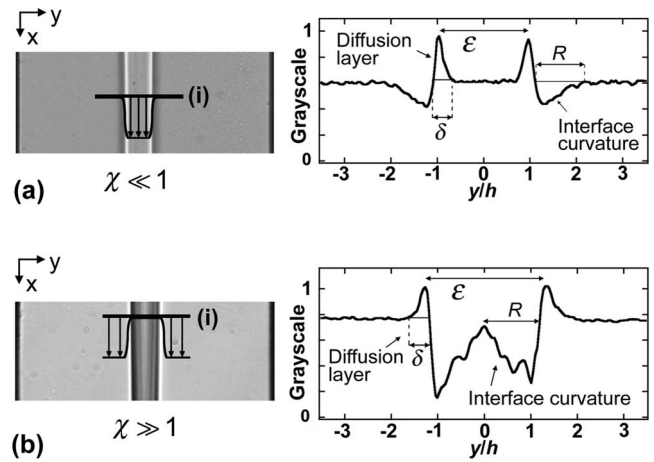

FIG. 3. Normalized grayscale profiles of miscible interfaces along the line (i) for (a) a less viscous central strip ($\chi=1/83$), and (b) a more viscous central strip ($\chi=122$). Light pixels represent diffusion area and dark pixels represent interface curvature. The central stream width is ε, the spread of the diffusion layer is δ, and the radius of curvature of the interface is R.

for precisely examining the width of the diffusion layer, we clearly observe that the lateral extension of a peak δ grows with x and decreases with Pe. This evidence suggests a direct correlation between the observed δ and the actual width of the diffusion layer that we assume alike for simplicity. When the x-y focus plane is located at the channel middle plane, peaks and valleys in the grayscale profile allow for determining the central stream width ε and for estimating the width of the diffusion layer δ. Valleys in the grayscale extend over a distance on the order the channel height $h=100 \, \mu m$, suggesting that the interface has a radius of curvature $R \sim h$. This $L1/L2$ interface curvature has a major effect on the flow microstructure when $\chi \gg 1$ for thin central streams $\varepsilon < 2h$. In this situation, the more viscous fluid can progressively detach from the top and bottom walls and becomes ensheathed, or lubricated by the less viscous liquid, thereby leading to the formation of a viscous thread. This lubrication process produces miscible contact lines that form a cusp at the detachment from the walls. The secondary bumps in the intensity profile of Fig. 3(b) suggest that these contact lines may be experimentally positioned at different locations on the top and on the bottom wall during the encapsulation process.

C. Central stream

Flow morphologies have been systematically investigated as a function of the viscosity ratio $\chi=\eta_1/\eta_2$ and the flow rate ratio $\varphi=Q_1/Q_2$. Figure 4 displays a composite image of superposed contour plots of the central stream for $\chi=122$ and for φ ranging between 2×10^{-4} and 10^{-1}. We observe that a steady-state viscous counterflow can be created. Indeed, for large central stream widths $\varepsilon/w \approx 1$, $L1$ flows upstream in the $L2$ channel, and, for small central stream widths $\varepsilon/w \ll 1$, $L2$ flows upstream in the $L1$ channel. In the four-phase contact region between $L1$, $L2$, glass, and silicon walls, the interface always locates itself at right angles to the sidewalls. This effect is evident with the circular channel geometry at
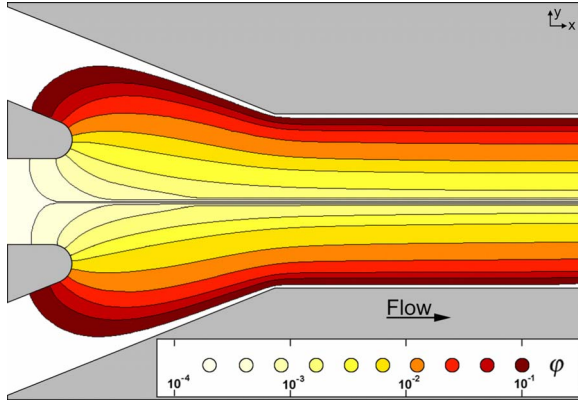
FIG. 4. (Color online) Contour plots of the measured central stream boundaries for $\chi = 122$ at various flow rate ratios φ. Miscible interfaces are perpendicular to solid sidewalls at the junction.
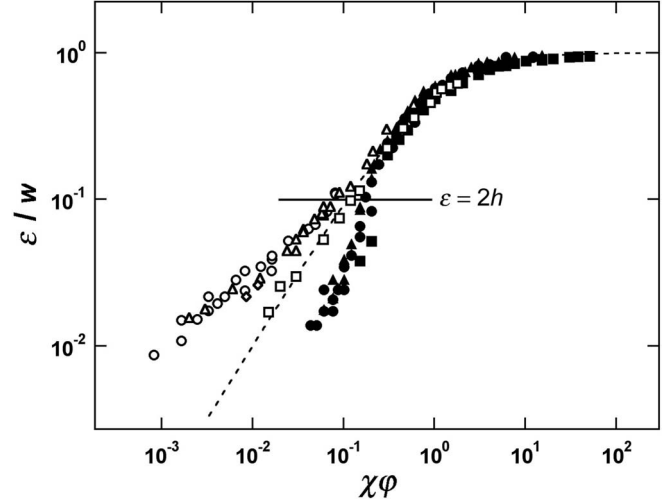

FIG. 5. Evolution of the normalized layer width ε/w with the dimensionless viscous stress ratio $\chi\varphi$. Dashed line, $\varepsilon/w = [1 + (\varphi\chi)^{-1}]^{-1}$. Viscosity ratio $\chi = 610$ (■), 122 (●), 61 (▲), 0.6 (□), 0.16 (◇), 1.2×10^{-2} (△), and 1.6×10^{-3} (○).

the inlet channel junctions (Fig. 4). Since the flows are laminar, they conform to the channel geometry over distances on the order of the largest length scale in the system w. In the absence of significant diffusion effects ($\delta \ll h$), we find from image processing that the evolution of the normalized stream width $\varepsilon(x)/w(x)$ along the x-axis, where x denotes the distance from the inlet channel junction, reaches a constant plateau with less than 10% variation at $x/w = 0.5$ in the converging channel for large streams, and less than 1% for all streams when $x/w > 2$. Therefore, in the outlet channel, flows are parallel and ε is essentially constant for $x > 2w$.

In the Hele-Shaw cell approximation, a flat $L1/L2$ interface is assumed for expressing the velocities of the streams in the outlet channel as a function of the flow rates in the inlet channels according to $U_1 = Q_1/(h\varepsilon)$ and $U_2 = Q_2/[h(w - \varepsilon)]$. In conjunction with Eq. (1), these relationships provide a direct estimate of the central stream width ε from the control parameters:

$$\varepsilon/w = [1 + (\varphi\chi)^{-1}]^{-1}. \tag{2}$$

In the absence of significant diffusion effects, this classic analytical solution [28,29] shows that ε increases monotonically with the dimensionless viscous stress ratio $\varphi\chi$. For χ ranging between 1.6×10^{-3} and 6.1×10^2, we measure ε at the location $x = 2w$ and find good agreement with Eq. (2) for $\varepsilon > 2h$ (Fig. 5). For $\varepsilon < 2h$ and viscosity ratios close to unity ($\chi = 0.6$), Eq. (2) also gives a good estimate of ε. However, we observe the separation of the experimental data into a lower branch for $\chi \gg 1$ and a higher branch for $\chi \ll 1$. The departure from Eq. (2) for large viscosity contrast is essentially due to $L1/L2$ interfacial curvature, which cannot be neglected for a small central stream of width $\varepsilon < 2R$.

D. Influence of diffusion

For low flow rates and/or large molecular diffusion coefficients, transverse diffusion can have considerable effects on the flow morphology. In order to gain insight into viscous encapsulation and ensheathing processes, we now focus on flow morphologies associated with $\chi \gg 1$ as a function of φ and the Péclet number Pe $= U^* h/D$, where $U^* = (U_1^* + U_2^*)/2$

is the mean interface velocity. Using Eq. (1), the interface velocity can be estimated such as $U^* = (1+\chi)U_1^*/2 \approx (\chi Q_1)/(2h\varepsilon)$. Using Eq. (2), this expression is reduced to $U^* \approx (\chi Q_1 + Q_2)/(2hw)$ for $\chi \gg 1$, and in this case, the Péclet number becomes

$$\text{Pe} = (\chi Q_1 + Q_2)/(2wD). \tag{3}$$

We observe that for low Pe $< 5 \times 10^3$, diffusion significantly "erodes" the central stream. The diffusion process locally decreases the viscosity contrast χ and produces a stream width ε, which is smaller than the prediction given by Eq. (2). This phenomenon, which may appear at first to be somewhat counterintuitive (e.g., since diffusion typically broadens the spread of the central stream), is apparent in Figs. 6(a) and 6(b) for fixed flow rate ratios and variable Pe. Diffusion can also facilitate viscous encapsulation by the sheath flow along the flow direction. For the diffusive regime, i.e., $\delta > h$, Fig. 6(c) shows the evolution of the grayscale profile along the flow path during the diffusion-enhanced encapsulation process. We experimentally observe the formation of a diffusion layer δ^* associated with this mechanism, as a double peak in the grayscale profile develops along the flow path. Evidence of the central stream's increase of curvature, and in turn encapsulation, is given by the reduction of the observed intensity of the stream grayscale for increasing x. The optical signature of the detachment of a thread corresponds to the merging of the valleys on either side of the central stream into one.

Grayscale analysis gives only partial information of the flow microstructure since it integrates the heterogeneous viscous region along the z axis. However, we measure the spread of the diffusive regions δ and δ^* as a function of X/Pe, where $X = x/h$ (Fig. 7). We find that for the weakly diffusive regime $\delta < h$, δ collapses on a single master curve fitted by $\delta/h = 2.5(X/\text{Pe})^{0.38}$. The exponent 0.38 is close to the theoretical value $1/3$ for $X/\text{Pe} \ll 1$. For the strongly dif-
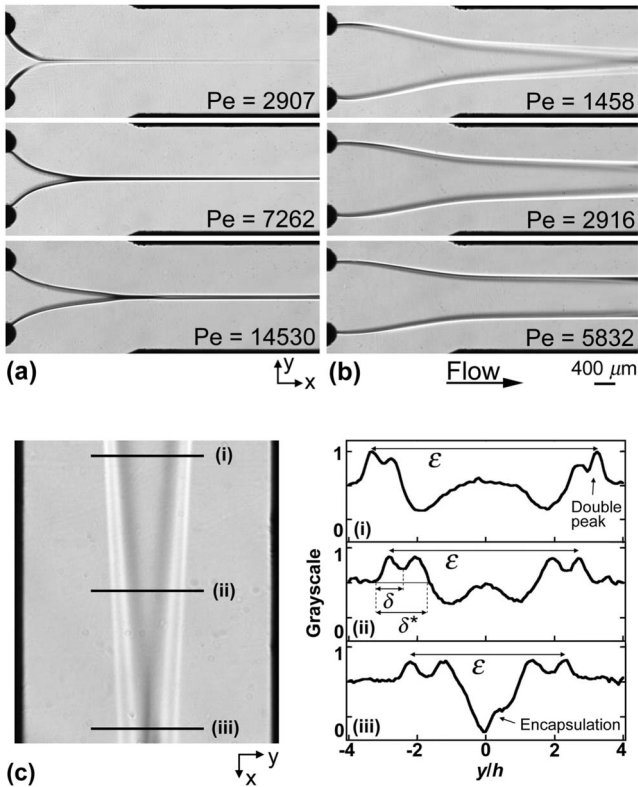
(a) **(b)** Flow▸ 400 μm

(c)

FIG. 6. Influence of the Péclet number on the formation of a central stream for $\chi = 122$. Flow rate ratio $\varphi = $ (a) 10^{-2} and (b) 5×10^{-3}. Diffusion erodes the more viscous stream, resulting in a decrease of the stream width ε. (c) Normalized grayscale profiles along the flow path $X = x/h$ for $\varphi = 5 \times 10^{-3}$ in strong diffusive regime with Pe=1458: $X =$ (i) 28, (ii) 39, and (iii) 50. Double peaks indicate the formation of a diffusion layer δ^* associated with the encapsulation process.

fusive regime, our limited experimental data suggest a scaling $\delta^*/h \propto (X/\text{Pe})^{1/2}$ similar to theory. Here, the cutoff value between the upstream and the downstream regions occurs for $X/\text{Pe} \approx 0.1$, which is far below the theoretical prediction
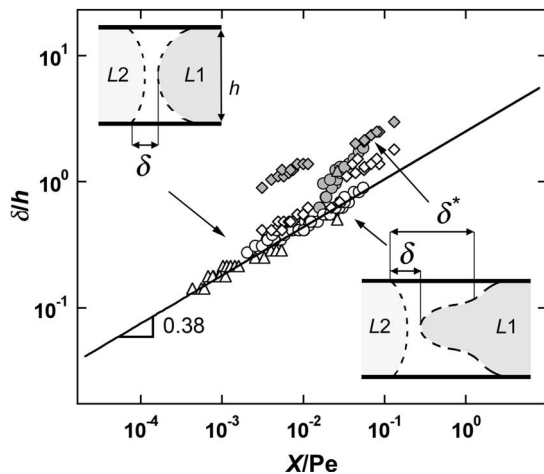

FIG. 7. Evolution of the normalized diffusion layer width δ/h with normalized distance X scaled by the Péclet number Pe. Open symbols, δ; solid symbols, δ^*. $\chi = 61$ ($\diamond$), 122 ($\bigcirc$), and 610 ($\triangle$).
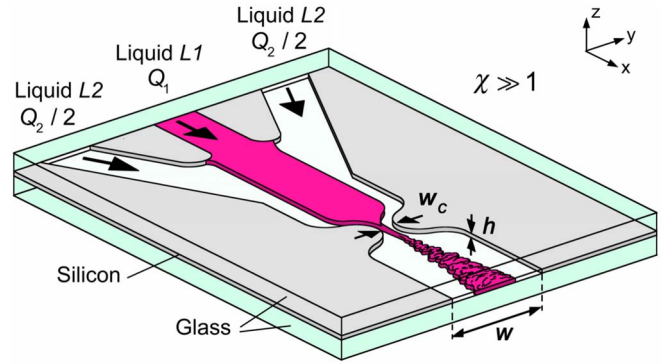

FIG. 8. (Color online) Schematic of hydrodynamic focusing in a plane geometry of height $h = 100$ μm and width $w = 2$ mm with a constriction of width $w_c = 200$ μm for large viscosity ratio $\chi \gg 1$.

$X/\text{Pe} \gg 1$. The dissociation of δ and δ^* gives evidence of the encapsulation process and occurs over relatively short distances. We find that δ^* increases with X/Pe in a fashion similar to a weakly diffusive regime when δ spreads predominantly near the top and bottom walls. In principle, the growth of δ^* in the downstream region would facilitate the envelopment of large streams (i.e., $\varepsilon > 2h$) in plane straight microgeometries having infinite length.

IV. CENTRAL STREAM WITH LARGE VISCOSITY RATIO IN A PLANE GEOMETRY WITH CONSTRICTION

Viscous flow-segregation processes depend dramatically on the channel aspect ratio w/h and can also be initiated by reducing the flow path with a constriction of width w_c. Constrictions are commonly used in microfluidic research to align elongated particles in suspension [38] and produce bubbles [39] or droplets [40] in continuous flows. Constrictions or throats are also relevant in natural geometries, such as in porous media, as conduits between pores [41]. Here, we use a circular constriction to avoid sharp corners that have a tendency to trap very viscous liquids or bubbles that can be introduced when refilling the injection syringes. Since encapsulation processes predominantly occur for small stream widths $\varepsilon < 2h$, we fabricate a plane hydrodynamic focusing microchannel which is identical to the geometry discussed above, yet also adds a constriction of width $w_c = 2h = 200$ μm located at a distance $L = 2w$ from the fluid contact region, such that $w(L) = w_c$ (Fig. 8).

A. Thread formation

For large viscosity contrasts $\chi \gg 1$, we observe "reversiblelike" flow behavior above a critical flow rate ratio $\varphi > \varphi_c$. In this regime, the flow direction is not readily distinguishable from the optical micrograph, there is no visible detachment and ensheathing of the more viscous liquid, and the system is characterized by similar flow morphologies upstream and downstream from the constriction [Fig. 9(a)]. As the miscible fluids flow through the constriction, the normalized stream width $\varepsilon(x)/w(x)$ remains approximately constant along the x axis according to the plane geometry assumption given by Eq. (2). However, when φ is decreased, oscillations
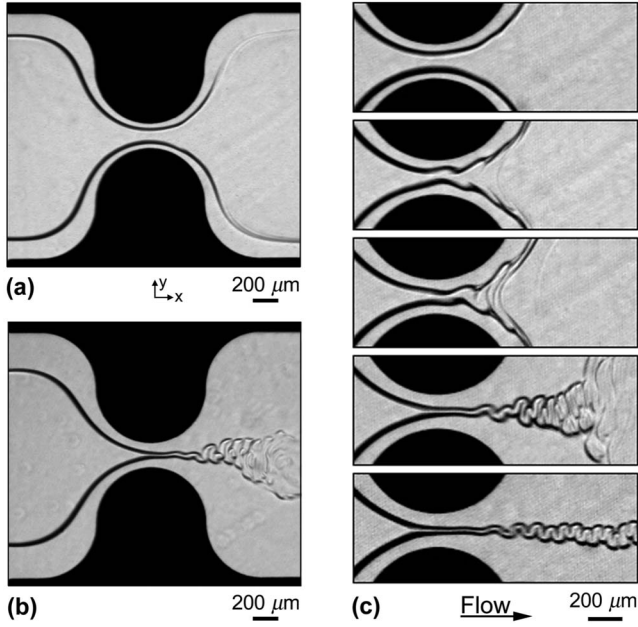
FIG. 9. Experimental micrographs of the viscous buckling transition in a constriction for $\chi=610$. Flow rates in $\mu l\ min^{-1}$. (a) Reversiblelike flow behavior, $Q_1=2$, $Q_2=60$. (b) Buckling of a viscous thread, $Q_1=2$, $Q_2=120$. (c) Onset of buckling for fixed $Q_1=1$, from top to bottom: $Q_2=22$, 24, 26, 28, and 30.

FIG. 10. Phase diagram of buckling transition with flow rate ratio φ versus Péclet number Pe for $\chi=61$ ($\bigcirc$), 122 ($\square$), and 610 ($\triangle$). The critical flow rate ratio φ_c (solid symbols) is fitted by the solid line: $\varphi_c=1.16Pe^{-0.34}$.

appear at the apex of constriction. These oscillations are convected downstream and result in a perturbation of the $L1/L2$ interface. As φ is further decreased toward φ_c, the oscillations grow in amplitude [Fig. 9(c)]. For $\varphi<\varphi_c$, the flow loses its reversiblelike behavior, and the morphologies upstream and downstream from the constriction differ significantly from one another [Fig. 9(b)]. This sharp transition strongly suggests that the high-viscosity fluid ($L1$) is encapsulated (i.e., ensheathed) by the low-viscosity fluid ($L2$), leading to the formation a viscous thread that is convected along in the flow of $L2$. Downstream from the constriction, the newly encapsulated viscous thread buckles instead of dilating. Indeed, contacting the top and bottom walls would cause $L1$ to experience a dramatic drop in velocity due to the large viscosity ratio χ. Therefore, the buckling of $L1$ initiated by the constriction gives a clear evidence of the viscous envelopment mechanism, corresponding to the complete detachment of $L1$ from the top and bottom walls.

B. Critical flow rate ratio

Upstream from the constriction, the flow is accelerated in the converging channel and Eq. (3) cannot be applied to estimate the Péclet number. Previous investigations in compact geometries (square microchannels) using miscible fluids in the absence of strong diffusion effects [18] as well as using immiscible fluids in the absence of significant capillary effects [42], showed that the viscous thread diameter ε depends only on the flow rate ratio φ for large χ. This situation is characterized by $L1$ being convected in plug flow within the parabolic flow of $L2$. In this case, the velocity contrast b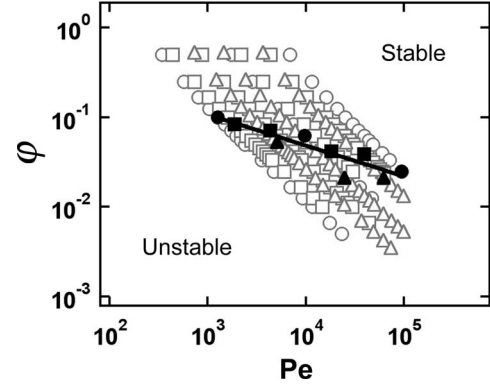etween the two fluids is negligible, and, at the apex of the constriction, the velocity at the interface is estimated by $U^*\approx(Q_1+Q_2)/(hw_c)$, which leads to a Péclet number Pe $\approx(Q_1+Q_2)/(w_cD)$. The critical flow rate ratio φ_c corresponding to the thread formation in the presence of the constriction, is measured as a function of Pe (Fig. 10). We find that φ_c decreases monotonically with Pe. The stability curve is fitted using $\varphi_c=aPe^b$, with $a=1.16$ and $b=-0.34$. We find that, even for large Péclet numbers Pe $>10^4$, molecular diffusion still plays a significant role and influences the stability of the flow.

C. Viscous buckling morphologies

Decelerated liquids jets display a broad and fascinating range of behaviors that depend on many parameters [43–45]. For instance, a viscous thread falling onto a surface can exhibit spontaneous oscillations and buckle by coiling or folding [46–49]. When combined with an external velocity, such as a moving surface [50,51], fluid buckling creates a vast array of morphologies with intricate interfaces. In microfluidic pressure-driven flows, the positioning of viscous threads by sheath flow allows for a great degree of control on the flow microstructure [19]. In the presence of large viscosity ratios, a diverging microchannel effectively provides a zone of transition between a compact geometry, characterized by a fast-moving lubricated thread, and a plane geometry, characterized by a layered flow with a slow-moving central stream. Downstream from the constriction, the thread impinges on and supplies a slowly convected, self-adjusting, more viscous pile. This convecting pile ultimately leaves the slit channel through an exit port far downstream.

A thread flowing from a straight square microchannel into a diverging channel exhibits an oscillation frequency f fixed by the effective shear rate (i.e., by the maximum fluid velocity) in the square channel [18]. For the case of a constriction, in addition to the primary folding mechanism, the thread position in the constriction can also periodically vary depending on the flow conditions. These variations typically occur at a frequency f_s much lower than the folding frequency, $f_s/f<10^{-1}$, and result in large changes to the pile's morphology (Fig. 11). Over the range of parameters investigated, these thread deformations are characterized by a "sec-
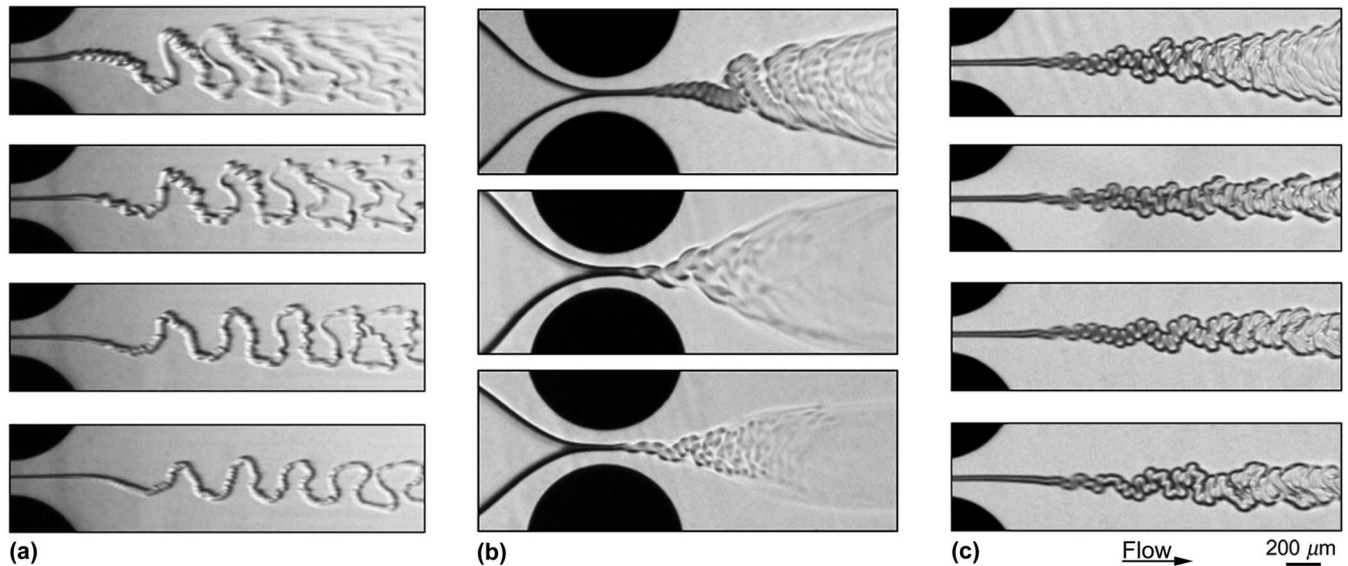
FIG. 11. Experimental micrographs of buckling instabilities downstream from the constriction. Flow rates in μl min^{-1}, from top to bottom. (a) Secondary coiling for $\chi=122$ and fixed $Q_1=2$: $Q_2=80$, $Q_2=120$, $Q_2=140$, $Q_2=180$. (b) Secondary coiling and folding for $\chi=61$, $Q_1=5$, $Q_2=80$, and for $\chi=610$ with fixed $Q_1=1$: $Q_2=28$, $Q_2=80$. (c) Secondary folding for $\chi=122$ and fixed $Q_1=10$: $Q_2=260$, $Q_2=280$, $Q_2=300$, $Q_2=320$.

ondary" coiling for low Pe $<5\times10^3$ [Fig. 11(a)], and a "secondary" folding for large Pe $>1.5\times10^4$ [Fig. 11(c)]. For secondary coiling, analysis of experimental movies reveals that portions of the thread along the x axis are convected at different velocities. This indicates that the thread is located at different positions along the z axis, and, therefore small induced oscillations produce the helical coils seen in the overall structure. Portions of a large secondary coiling thread can contact the top and bottom plates, thereby producing highly complex viscous patterns [Fig. 11(a), top]. For secondary folding, the thread is mainly restricted to deform in the x-y plane. Hybrid secondary coiling and folding regimes are also observed [Fig. 11(b)].

In addition to the Péclet number Pe and the viscosity ratio χ, we find that the fluid driving mechanism also plays a role in the flow selection. Small pulses created by the mechanical syringe pumps are suspected to initiate secondary coiling, in particular for small flow rates. However, preliminary experiments performed with fluids injected from pressurized reservoirs show that secondary deformations also occur. Here, the combination of high natural buckling frequency with the modulation of a low forcing frequency leads to microflows that have remarkable morphologies.

V. CONCLUSION

In this paper, we have examined symmetric hydrodynamic focusing in plane microgeometries to experimentally study miscible two-fluid flows having large viscosity contrasts. Continuous flows, when controlled in designed microfluidic geometries, provide a means for creating and manipulating steady and oscillatory miscible fluid interfaces. In particular, we have shown that, due to the large viscosity contrast, the boundary associated with more viscous stream is convex. We have measured the width of the central stream as a function of fluid properties and flow parameters, and we find that less viscous liquid can envelop a more viscous central stream to form a viscous thread. For the weakly diffusive regime, the evolution of the diffusion layer agrees well with theoretical predictions made in the absence of large viscosity contrasts. When the transverse spread of the diffusion layer is comparable to the plate gap, we have demonstrated that diffusion can enhance self-lubrication processes. The adjunction of a small constriction into the flow path facilitates the formation of viscous threads at relatively large flow rate ratios. We have studied the influence of the Péclet number on the critical flow rate ratio for thread formation, and we have discovered and described novel kinds of viscous buckling morphologies downstream from the constriction. Small variations of the thread position in the constriction, due to perturbations in the driving flows, lead to secondary thread deformations that create a wide range of miscible fluid microstructures.

The phenomena associated with viscous flow-segregation offer innovative mechanisms for microfluidic manipulation of miscible interfaces and for passively blending small amounts of high- and low-viscosity fluids. Control of viscous stratifications in microsystems is particularly promising for thick material transport, synthesis, and characterization using continuous pressure-driven flows. The formation and evolution of viscous threads in the presence of well-controlled flow fields provide simple experimental models for investigating fluid interactions far from equilibrium. Complementary numerical and theoretical investigations on viscous sequestration and buckling in microgeometries would enable better predictions of reactive multifluid flows of widely different liquid-borne species. Successful development of integrated microfluidic systems places increasing demands on understanding viscous multifluid flow behaviors associated with transitions between plane and compact geometries. The

ability to initiate self-lubrication processes at such small scales provides an interesting alternative for reducing the energy needed to pump and manipulate thick materials in nanoscale environments.

[1] T. J. Squires and S. R. Quake, Rev. Mod. Phys. **77**, 977 (2005).

[2] A. Günther and K. F. Jensen, Lab Chip **6**, 1487 (2006).

[3] S. Y. Teh, R. Lin, L.-H. Hung, and A. P. Lee, Lab Chip **8**, 198 (2008).

[4] M. A. Holden, S. Kumar, E. T. Castellana, A. Beskok, and P. S. Cremer, Sens. Actuators B **92**, 199 (2003).

[5] J. Goulpeau, B. Lonetti, D. Trouchet, A. Ajdari, and P. Tabeling, Lab Chip **7**, 1154 (2007).

[6] W. Georgescu, J. Jourquin, L. Estrada, A. R. A. Anderson, V. Quanrata, and J. P. Wikswo, Lab Chip **8**, 238 (2008).

[7] J. Ottino and S. Wiggins, Philos. Trans. R. Soc. London, Ser. A **362**, 923 (2004).

[8] N. T. Nguyen and Z. Wu, J. Micromech. Microeng. **15**, R1 (2005).

[9] N. Kockmann, T. Kiefer, M. Engler, and P. Woias, Sens. Actuators B **117**, 495 (2006).

[10] C. S. Yih, J. Fluid Mech. **27**, 337 (1967).

[11] C. E. Hickox, Phys. Fluids **14**, 251 (1971).

[12] Q. Cao, A. L. Ventresca, K. R. Sreenivas, and A. K. Prasad, Can. J. Chem. Eng. **81**, 913 (2003).

[13] B. Selvam, S. Merk, R. Govindarajan, and E. Meiburg, J. Fluid Mech. **592**, 23 (2007).

[14] G. M. Homsy, Annu. Rev. Fluid Mech. **19**, 271 (1987).

[15] E. Lajeunesse, J. Martin, N. Rakotomalala, D. Salin, and Y. C. Yortos, J. Fluid Mech. **398**, 299 (1999).

[16] N. Rashidnia, R. Balasubramaniam, and R. T. Schroer, Ann. N.Y. Acad. Sci. **1027**, 311 (2004).

[17] S. H. Vanaparthy and E. Meiburg, Eur. J. Mech. B/Fluids **27**, 268 (2008).

[18] T. Cubaud and T. G. Mason, Phys. Rev. Lett. **96**, 114501 (2006).

[19] T. Cubaud and T. G. Mason, Phys. Rev. Lett. **98**, 264501 (2007).

[20] D. D. Joseph, K. Nguyen, and G. S. Beavers, J. Fluid Mech. **141**, 319 (1984).

[21] D. D. Joseph and Y. Y. Renardy, *Fundamentals of Two-Fluid Dynamics. Part II: Lubricated Transport, Drops and Miscible Liquids* (Springer-Verlag, New York, 1993).

[22] B. Khomami and K. C. Su, J. Non-Newtonian Fluid Mech. **91**, 59 (2000).

[23] J. B. Knight, A. Vishwanath, J. P. Brody, and R. H. Austin, Phys. Rev. Lett. **80**, 3863 (1998).

[24] G. B. Lee, C. C. Chang, S. B. Huang, and R. J. Yang, J. Micromech. Microeng. **16**, 1024 (2006).

[25] C. Simonet and A. Groisman, Appl. Phys. Lett. **87**, 114104 (2005).

[26] C. C. Chang, Z. X. Huang, and R. Y. Yang, J. Micromech. Microeng. **17**, 1479 (2007).

[27] T. Stiles, R. Fallon, T. Vestad, J. Oakey, D. W. M. Marr, J. Squier, and R. Jimenez, Microfluid. Nanofluid. **1**, 280 (2005).

[28] Z. Wu and N.-T. Nguyen, Sens. Actuators B **107**, 965 (2005).

[29] M. U. Larsen and N. C. Shapley, Anal. Chem. **79**, 1947 (2007).

[30] R. F. Ismagilov, A. D. Stroock, P. J. A. Kenis, G. Whitesides, and H. A. Stone, Appl. Phys. Lett. **76**, 2376 (2000).

[31] J. Jiménez, J. Fluid Mech. **535**, 245 (2005).

[32] J. B. Salmon and A. Ajdari, J. Appl. Phys. **101**, 074902 (2007).

[33] N. Rashidnia, R. Balasubramaniam, J. Kuang, P. Petitjeans, and T. Maxworthy, Int. J. Thermophys. **22**, 547 (2001).

[34] F. Ould-Kaddour and D. Levesque, Phys. Rev. E **63**, 011205 (2000).

[35] T. Konishi, T. Yoshizaki, and H. Yamakawa, Macromolecules **24**, 5614 (1991).

[36] Z. Zhou and D. Yan, Macromol. Theory Simul. **6**, 161 (1997).

[37] P. Gondret and M. Rabaud, Phys. Fluids **9**, 3267 (1997).

[38] E. Katz, A. L. Yarin, W. Salalha, and E. Zussman, J. Appl. Phys. **100**, 034313 (2006).

[39] P. Garstecki, H. A. Stone, and G. W. Whitesides, Phys. Rev. Lett. **94**, 164501 (2005).

[40] S. L. Anna, N. Bontoux, and H. A. Stone, Appl. Phys. Lett. **82**, 364 (2003).

[41] M. Sahimi, Rev. Mod. Phys. **65**, 1393 (1993).

[42] T. Cubaud and T. G. Mason, Phys. Fluids **20**, 053302 (2008).

[43] J. Eggers and E. Villermaux, Rep. Prog. Phys. **71**, 036601 (2008).

[44] A. I. Pesci, M. A. Porter, and R. E. Goldstein, Phys. Rev. E **68**, 056305 (2003).

[45] C. Dombrowski, B. Lewellyn, A. I. Pesci, J. M. Restrepo, J. O. Kessler, and R. E. Goldstein, Phys. Rev. Lett. **95**, 184501 (2005).

[46] J. O. Cruickshank and B. R. Munson, J. Fluid Mech. **113**, 221 (1981).

[47] R. W. Griffiths and J. S. Turner, Geophys. J. **95**, 397 (1988).

[48] M. Skorobogatiy and L. Mahadevan, Europhys. Lett. **52**, 532 (2000).

[49] M. Maleki, M. Habibi, R. Golestanian, N. M. Ribe, and D. Bonn, Phys. Rev. Lett. **93**, 214502 (2004).

[50] S. Chiu-Webster and J. R. Lister, J. Fluid Mech. **569**, 89 (2006).

[51] N. M. Ribe, J. R. Lister, and S. Chiu-Webster, Phys. Fluids **18**, 124105 (2006).